Supplement of Atmos. Chem. Phys., 18, 7149–7168, 2018
https://doi.org/10.5194/acp-18-7149-2018-supplement

Supplement of

Influence of intense secondary aerosol formation and long-range transport on aerosol chemistry and properties in the Seoul Metropolitan Area during spring time: results from KORUS-AQ

Hwajin Kim et al.

Correspondence to: Qi Zhang (dkwzhang@ucdavis.edu)

Tables

Table S1. Average (± 1 standard deviation), minimum and maximum concentrations of the particulate matter (PM_1) species and the total PM_1 mass over the whole campaign, and the average contribution of each of the PM_1 species to the total PM_1 mass.

	Average conc. ± one standard deviation ($\mu g\ m^{-3}$)	5th percentile conc. ($\mu g\ m^{-3}$)	95th percentile conc. ($\mu g\ m^{-3}$)	Fraction of total PM_1 (%)	Detection limit (3min) ($\mu g\ m^{-3}$)
Organics	9.76 ± 5.27	3.12	19.3	44	0.04
Nitrate	3.78 ± 4.20	0.33	13.4	17	0.01
Sulfate	4.40 ± 3.26	1.10	11.0	20	0.01
Ammonium	2.56 ± 2.16	0.53	7.46	12	0.03
Chloride	0.04 ± 0.05	ND	0.14	0	0.01
Black carbon	1.52 ± 0.82	0.44	2.94	7	0.1
Total PM_1	22.1 ± 13.0	6.79	50.1	100	0.05

Table S2. Correlation coefficient (Pearson's r) for the linear regressions between organic aerosol (OA) factors (including the sum of primary factors (primary OA (POA) = hydrocarbon like OA (HOA) + cooking OA (COA) + biomass burning OA (BBOA)), as well as the sum of the oxidized factors (oxidized OA (OOA) = semi-volatile OOA (SV-OOA) + low volatile (LV-OOA)), and various particle- and gas-phase species, and ions.

r	**HOA**	**COA**	**POA (HOA+ COA)**	**SV-OOA**	**LV-OOA**	**OOA (SV-OOA+ LV-OOA)**
Nitrate	0.28	0.13	0.23	0.21	0.02	0.11
Sulfate	0.05	-0.05	0.00	-0.06	-0.03	-0.04
Ammonium	0.19	0.04	0.12	0.07	0.00	0.03
Chloride	0.47	0.13	0.32	0.05	-0.10	-0.05
K (AMS)	0.50	**0.68**	**0.70**	**0.73**	0.55	**0.70**
Primary pollutants						
BC	0.54	0.38	0.52	0.42	0.22	0.34
CO	0.36	0.30	0.38	0.23	0.03	0.12
NO_2	0.41	0.57	0.58	0.27	0.13	0.21
AMS tracer ions (*m/z* value)						
CO_2^+ (44)	0.22	0.31	0.31	0.61	**0.78**	**0.80**
$C_2H_5N^+$ (43)	0.10	0.18	0.17	0.64	0.58	0.68
$C_2H_4O_2^+$ (60)	0.39	0.62	0.60	**0.67**	**0.75**	**0.81**
$C_3H_5O_2^+$ (73)	0.35	0.61	0.58	**0.66**	**0.81**	**0.85**
$C_3H_3O^+$ (55)	0.39	**0.75**	**0.69**	**0.73**	**0.67**	**0.78**
$C_3H_5O^+$ (57)	0.37	0.61	0.59	**0.79**	**0.75**	**0.87**
$C_3H_7^+$ (43)	**0.87**	**0.80**	**0.97**	0.43	0.17	0.31
$C_3H_7N^+$ (57)	0	0.06	0.04	0.26	0.33	0.34
$C_4H_7^+$ (55)	**0.85**	**0.78**	**0.98**	0.52	0.24	0.40
$C_4H_9^+$ (43)	**0.81**	**0.84**	**0.96**	0.42	0.00	0.24
$C_5H_{11}^+$ (57)	**0.96**	0.60	**0.89**	0.28	0.04	0.15
$C_5H_8O^+$ (84)	0.46	**0.89**	**0.82**	0.60	0.41	0.55
$C_6H_{10}O^+$ (98)	0.46	**0.96**	**0.87**	0.38	0.20	0.31
$C_7H_{12}O^+$ (112)	0.40	**0.70**	**0.66**	0.44	0.30	0.41
$C_9H_7^+$ (115)	0.54	**0.71**	**0.74**	**0.72**	0.59	**0.73**
CHN^+ (27)	0.23	0.25	0.28	0.37	0.47	0.49
CN^+ (26)	0.15	0.29	0.26	0.11	0.08	0.11
$CH_2SO_2^+$ (77)	0.20	0.09	0.16	0.06	0.04	0.05
$CH_3SO_2^+$ (78)	0.21	0.09	0.17	0.05	0.03	0.04

BC, black carbon; AMS, aerosol mass spectrometer; PAH, polycyclic aromatic hydrocarbons

Value that are r > 0.7 are boldfaced

Table S3. Comparison of the average O/C, H/C, and OM/OC ratios of total OA and the four OA factors identified from PMF analysis calculated using the Aiken-Ambient method (Aiken et al., 2008) and the improved Canagaratna-Ambient method (Canagaratna et al., 2015).

Species	Ratio	Aiken-Ambient	Canagaratna-Ambient
OA	O/C	0.38	0.49
	H/C	1.52	1.67
	OM/OC	1.66	1.82
HOA	O/C	0.11	0.15
	H/C	1.85	2.00
	OM/OC	1.31	1.37
COA	O/C	0.15	0.19
	H/C	1.68	1.83
	OM/OC	1.34	1.41
SVOOA	O/C	0.33	0.44
	H/C	1.55	1.73
	OM/OC	1.58	1.74
LVOOA	O/C	0.51	0.91
	H/C	1.41	1.46
	OM/OC	1.84	2.36

Table S4. Comparison of aerosol properties and meteorological parameters at different stages during haze period.

	Overall	**S1**	**S2**	**S3**	**S4**
Average non-refractory submicrometer particulate matter (NR-PM_1) mass concentration ($\mu g\ m^{-3}$) (Average)	22.1	9.0	41.2	37.7	13.0
RH(%) / Temp(°C)	62/19	96/16	78/18	67/21	48/23
WS(m/s)	1.7	3.0	2.2	1.4	1.7
Trace gas conc.(CO (ppm) and /SO_2/ NO_2 O_3/(ppb))	0.52/5.1/34/29	0.48/4.0/39/15	0.55/4.8/32/39	0.62/6.1/37/35	0.39/4.5/28.7/33

PM, particulate matter; NR-PM_1, non-refractory submicrometer particulate matter; RH, relative humidity

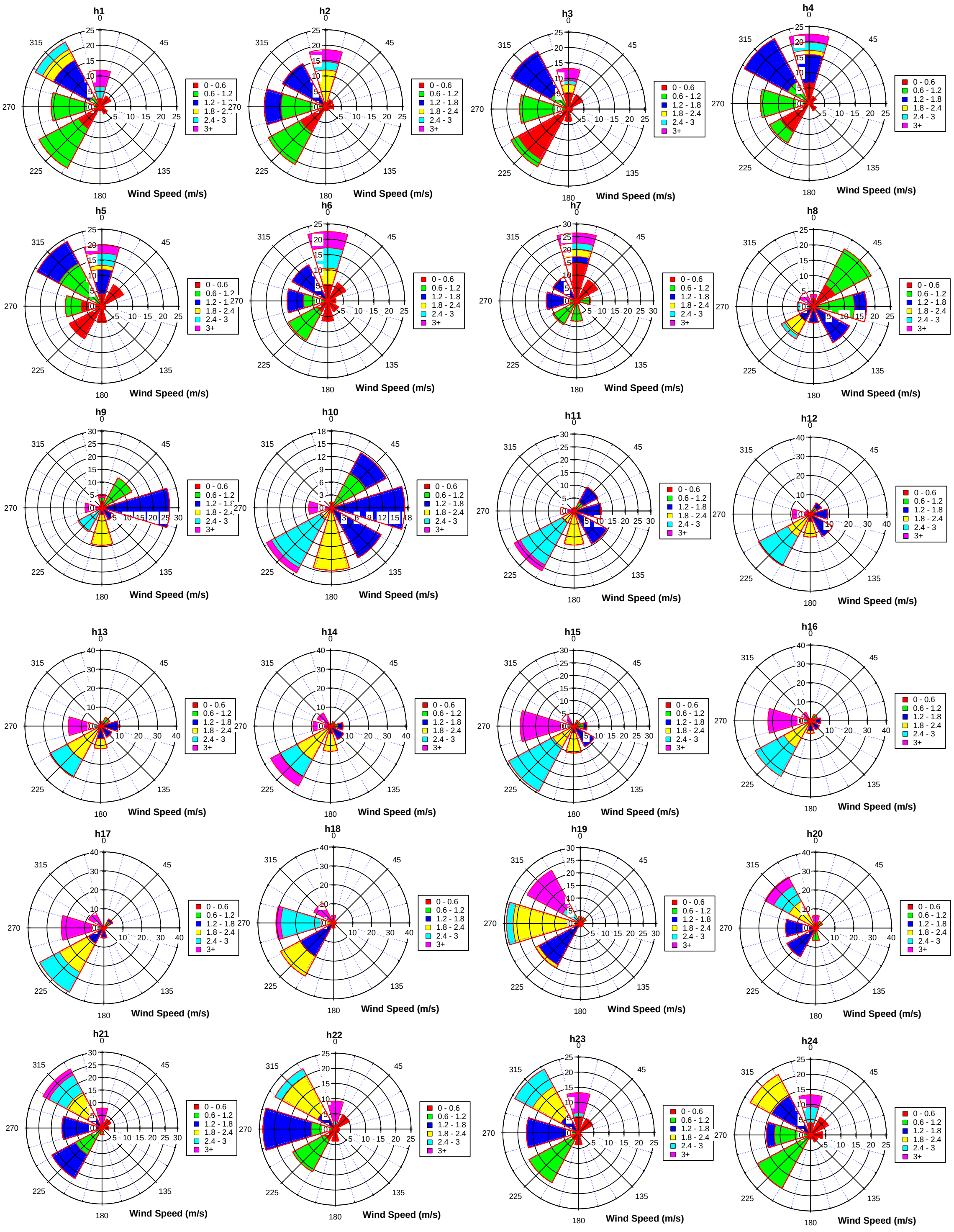

Figure S1. Wind Rose plots for every hour colored by wind speed. Radial scales correspond to the frequency.

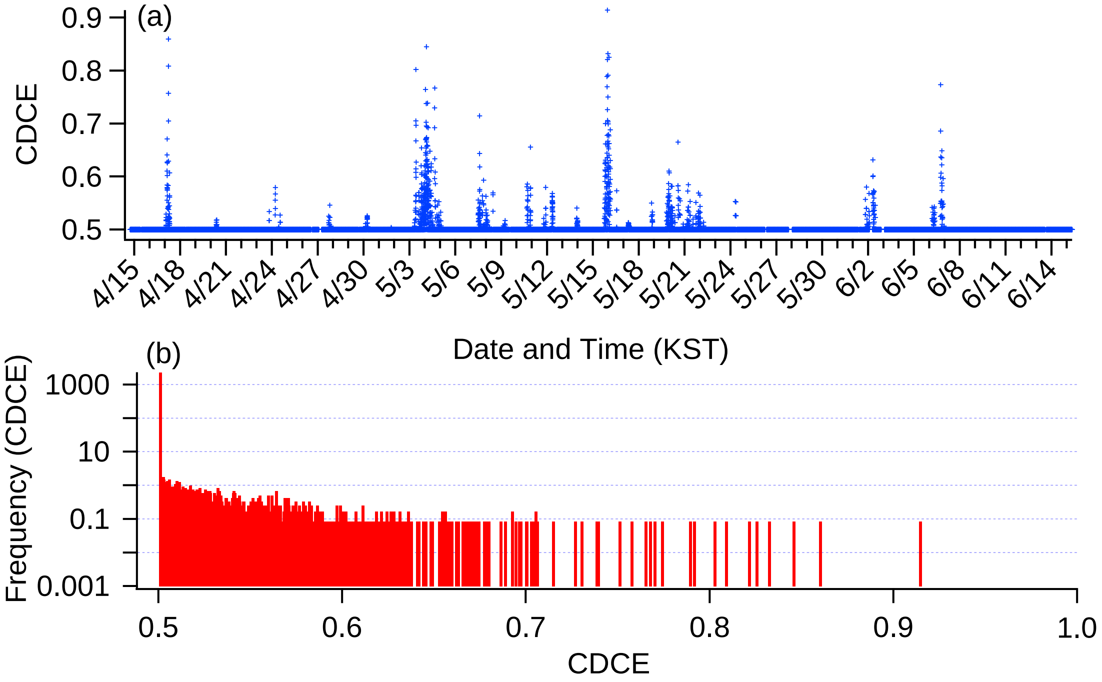

Figure S2. (a) Time series of composition dependent collection efficiency (CDCE) and; **(b)** histogram of CDCE, averaging 0.5 ± 0.01.

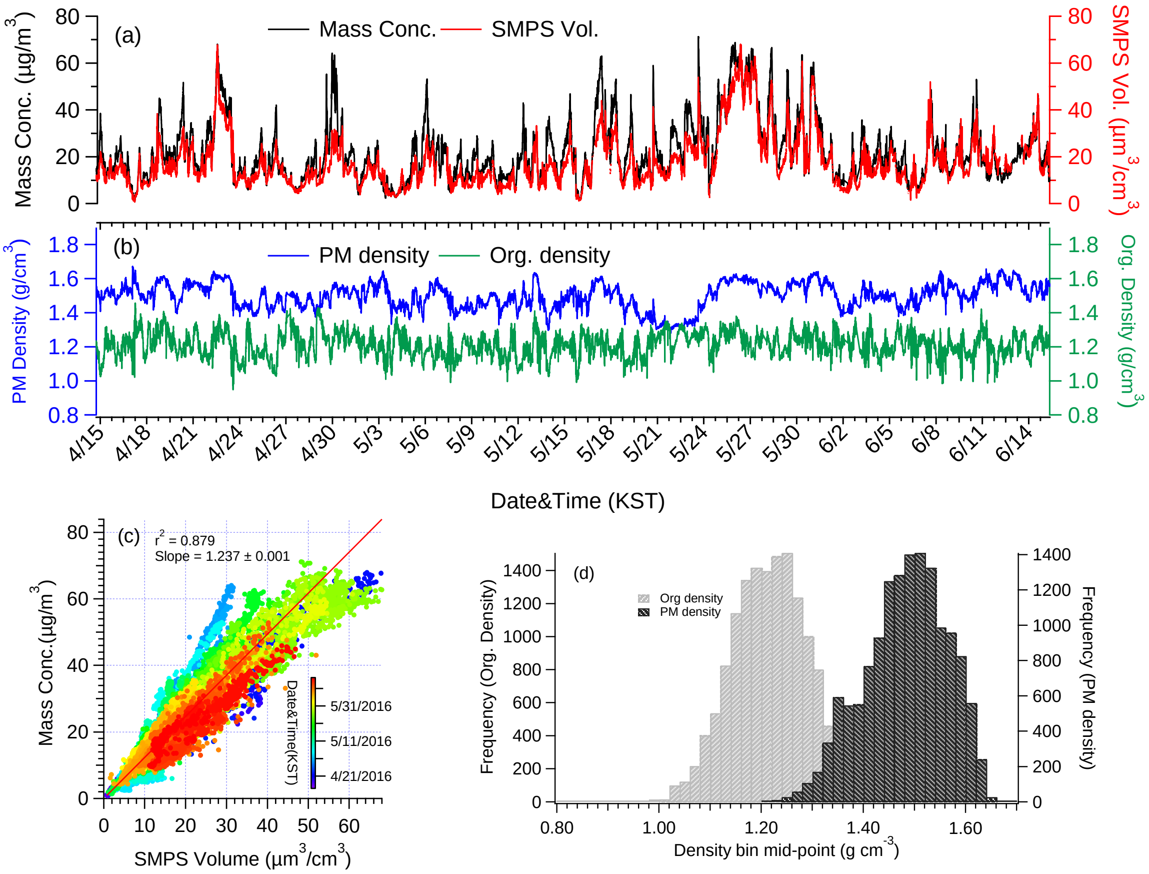

Figure S3. (a) Time series of total particulate matter (PM_1) and scanning mobility particle sizer (SMPS) volume concentrations. The correlation and ratio between PM_1 and $PM_{2.5}$ are shown ; **(b)** Time series of the organic aerosol density estimated using the method reported in Kuwata et al. (2012)

$$\rho_{org} = [12 + 1\bullet(H/C) + 16\bullet(O/C)]/\ [7 + 5\bullet(H/C) + 4.15\bullet(O/C)]$$

and bulk aerosol density estimated from the measured chemical composition, known inorganic species density and the organic density estimated above (Zhang et al., 2005). **(c)** Scatter plot of the total PM_1 mass (NR-PM_1 plus BC) versus SMPS volume, where the NR-PM_1 mass concentrations have been determined using the composition-dependent collection efficiencies; **(d)** histogram of organic aerosol density (average = 1.21 g cm^{-3}) and bulk aerosol density (average = 1.5 g cm^{-3}).

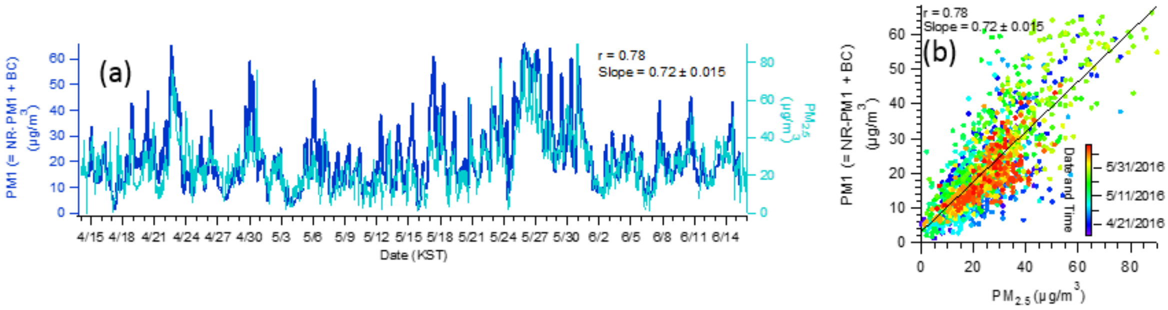

Figure S4. (a) Time series of total particulate matter (PM$_1$) concentration and PM$_{2.5}$ mass concentration measured at Gireum sitel (b) Scatter plot of total PM$_1$ mass (NR-PM$_1$ plus BC) versus PM$_{2.5}$ mass.

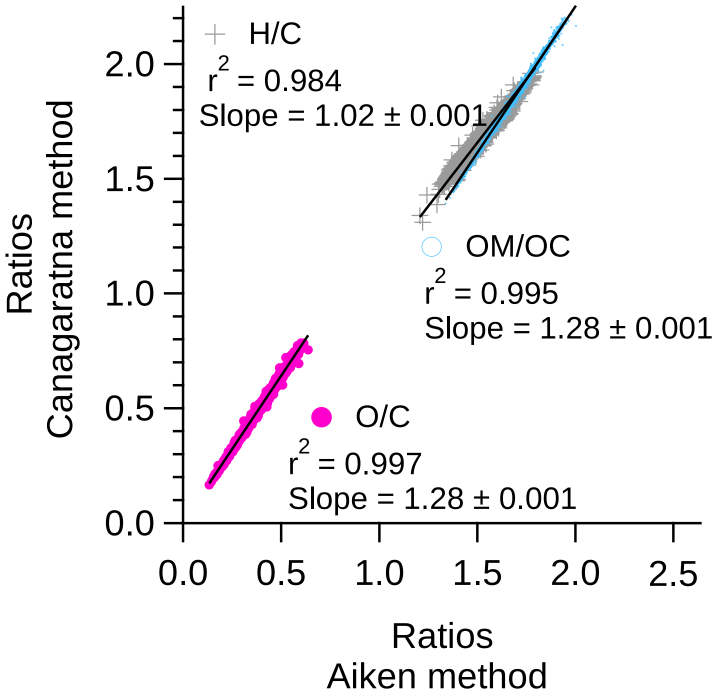

Figure S5. Scatter plot of OM/OC, O/C, and H/C calculated with the Canagaratna method vs. those with the Aiken-Ambient method.

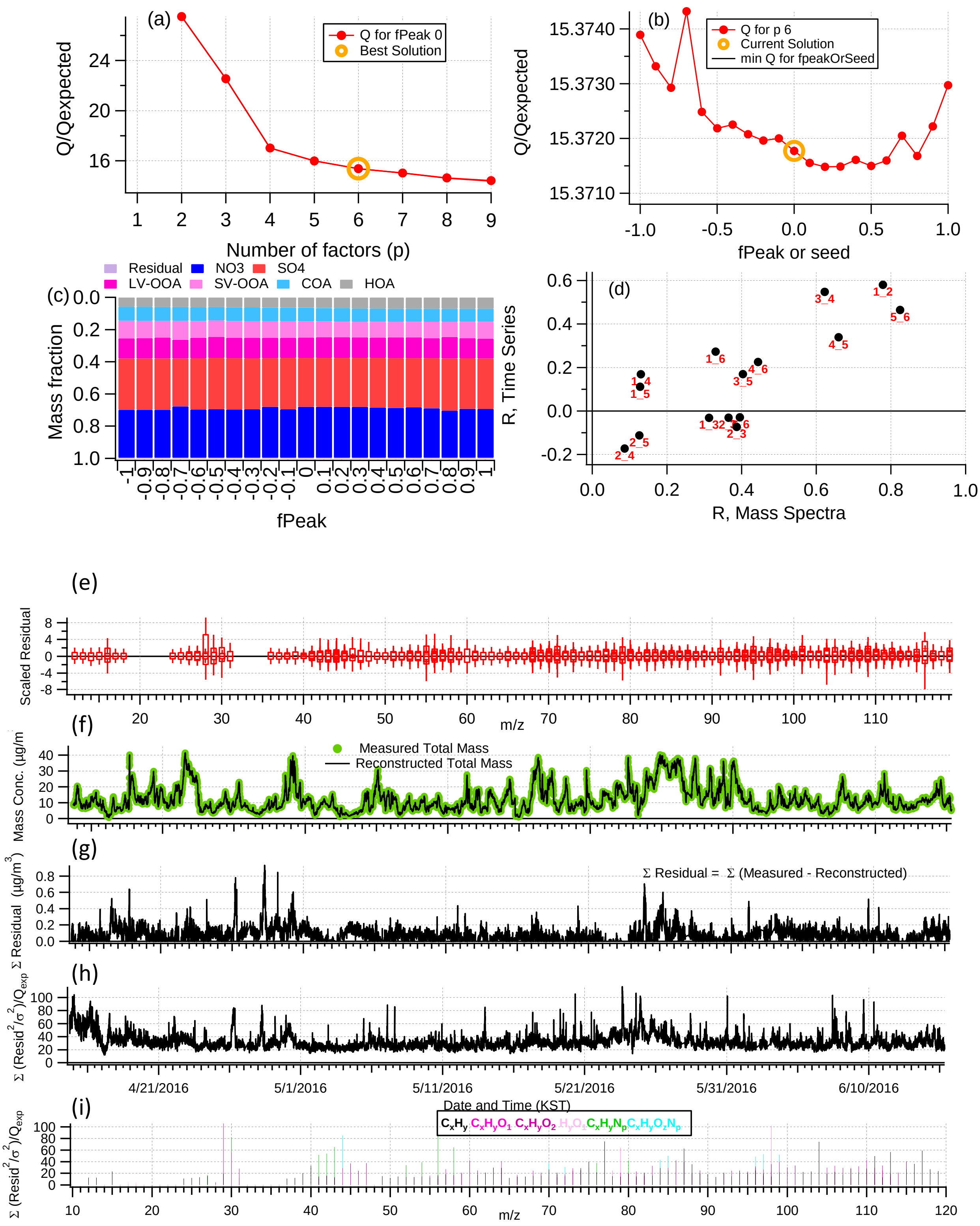
(a)
Q for fPeak 0
Best Solution
Q/Qexpected
24
20
16
1 2 3 4 5 6 7 8 9
Number of factors (p)
(b)
Q for p 6
Current Solution
min Q for fpeakOrSeed
Q/Qexpected
15.3740
15.3730
15.3720
15.3710
-1.0 -0.5 0.0 0.5 1.0
fPeak or seed
(c)
Residual NO3 SO4
LV-OOA SV-OOA COA HOA
Mass fraction
0.0 0.2 0.4 0.6 0.8 1.0
-1 -0.9 -0.8 -0.7 -0.6 -0.5 -0.4 -0.3 -0.2 -0.1 0 0.1 0.2 0.3 0.4 0.5 0.6 0.7 0.8 0.9 1
fPeak
(d)
R, Time Series
0.6 0.4 0.2 0.0 -0.2
3_4 1_2 5_6 4_5 1_6 4_6 3_5 1_4 1_5 1_3 2_6 2_3 2_5 2_4
0.0 0.2 0.4 0.6 0.8 1.0
R, Mass Spectra
(e)
Scaled Residual
8 4 0 -4 -8
20 30 40 50 60 70 80 90 100 110
m/z
(f)
Mass Conc. (μg/m
40 30 20 10 0
Measured Total Mass
Reconstructed Total Mass
(g)
Σ Residual (μg/m^3)
0.8 0.6 0.4 0.2 0.0
Σ Residual = Σ (Measured - Reconstructed)
(h)
Σ (Resid^2/σ^2)/Q$_{exp}$
100 80 60 40 20 0
4/21/2016 5/1/2016 5/11/2016 5/21/2016 5/31/2016 6/10/2016
Date and Time (KST)
(i)
Σ (Resid^2/σ^2)/Q$_{exp}$
100 80 60 40 20 0
C$_x$H$_y$ C$_x$H$_y$O$_1$ C$_x$H$_y$O$_2$ H$_y$O$_z$ C$_x$H$_y$N$_p$ C$_x$H$_y$O$_z$N$_p$
10 20 30 40 50 60 70 80 90 100 110 120
m/z

Figure S6. Summary of the key diagnostic plots of the chosen 6-factor solution (4 OA factor solution) from PMF analysis of the organic aerosol fraction: **(a)** Q/Q_{exp} as a function of the number of factors (p) explored in PMF analysis, with the best solution denoted by the open orange circle. Plots **b-i** are for the chosen solution set, containing 4 factors: **(b)** Q/Q_{exp} as a function of fPeak; **(c)** mass fractional contribution to the total mass of each of the PMF factors, including the residual (in purple), as a function of fPeak; **(d)** Pearson's r correlation coefficient values for correlations among the time series and mass spectra of the PMF factors. Here, 1 = NO_3, 2 = SO_4, 3 = LV-OOA, 4 = SV-OOA, 5 = COA, 6 = HOA; **(e)** box and whiskers plot showing the distributions of scaled residuals for each *m/z*; **(f)** time series of the measured mass and the reconstructed mass from the sum of the 6 factors; **(g)** time series of the variations in the residual (= measured – reconstructed) of the fit; **(h)** the Q/Q_{exp} for each point in time; **(i)** the Q/Q_{exp} values for each fragment ion.

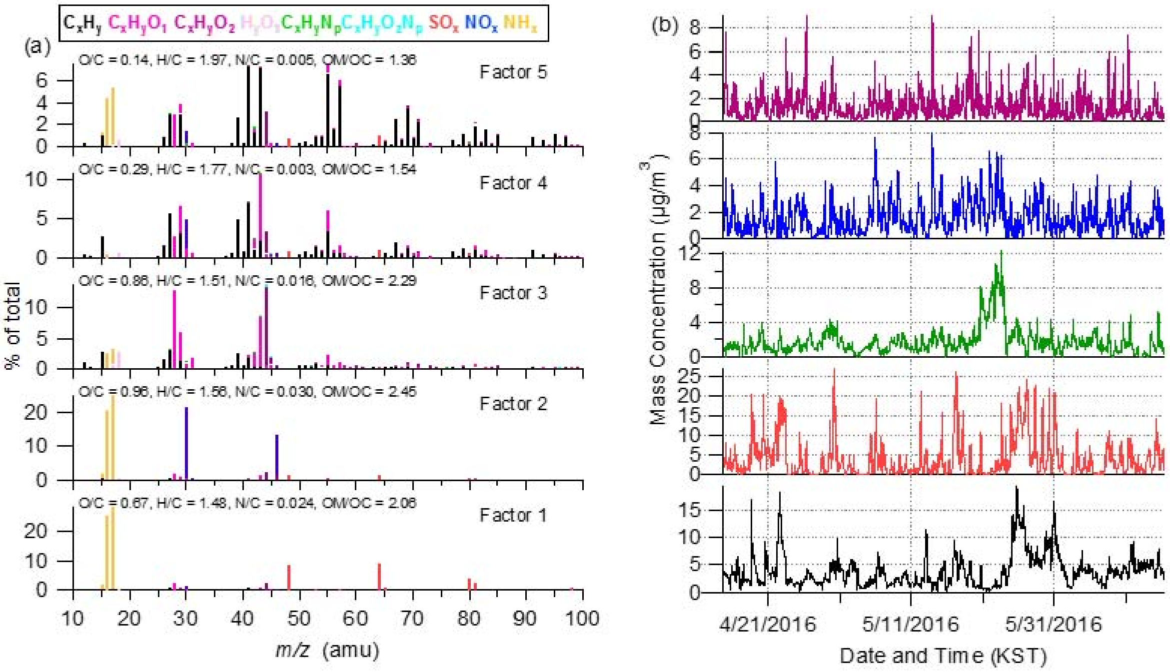

C_xH_y $C_xH_yO_1$ $C_xH_yO_2$ H_yO_1 $C_xH_yN_p$ $C_xH_yO_zN_p$ SO_x NO_x NH_x
(a)
O/C = 0.14, H/C = 1.97, N/C = 0.005, OM/OC = 1.36
Factor 5
O/C = 0.29, H/C = 1.77, N/C = 0.003, OM/OC = 1.54
Factor 4
O/C = 0.86, H/C = 1.51, N/C = 0.016, OM/OC = 2.29
Factor 3
O/C = 0.96, H/C = 1.56, N/C = 0.030, OM/OC = 2.45
Factor 2
O/C = 0.67, H/C = 1.48, N/C = 0.024, OM/OC = 2.06
Factor 1
% of total
10 20 30 40 50 60 70 80 90 100
m/z (amu)
(b)
Mass Concentration (µg/m^3)
4/21/2016
5/11/2016
5/31/2016
Date and Time (KST)

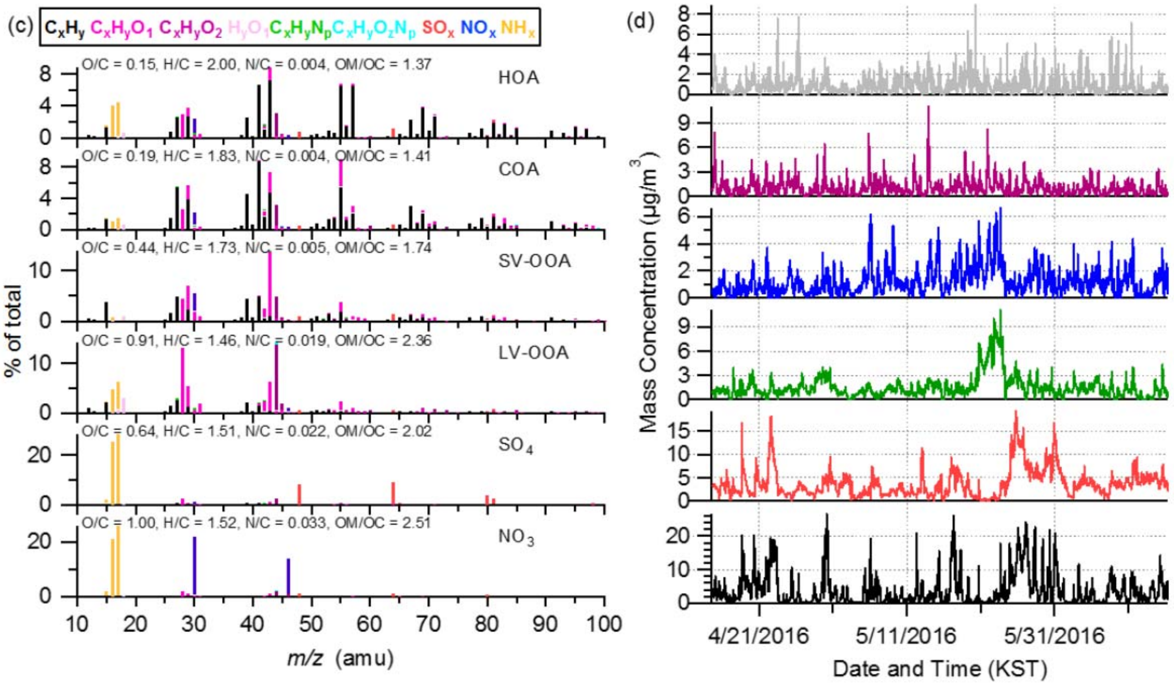

(c)
C_xH_y $C_xH_yO_1$ $C_xH_yO_2$ H_yO_1 $C_xH_yN_p$ $C_xH_yO_zN_p$ SO_x NO_x NH_x
O/C = 0.15, H/C = 2.00, N/C = 0.004, OM/OC = 1.37
HOA
O/C = 0.19, H/C = 1.83, N/C = 0.004, OM/OC = 1.41
COA
O/C = 0.44, H/C = 1.73, N/C = 0.005, OM/OC = 1.74
SV-OOA
O/C = 0.91, H/C = 1.46, N/C = 0.019, OM/OC = 2.36
LV-OOA
O/C = 0.64, H/C = 1.51, N/C = 0.022, OM/OC = 2.02
SO_4
O/C = 1.00, H/C = 1.52, N/C = 0.033, OM/OC = 2.51
NO_3
% of total
10 20 30 40 50 60 70 80 90 100
m/z (amu)
(d)
Mass Concentration (µg/m^3)
4/21/2016
5/11/2016
5/31/2016
Date and Time (KST)

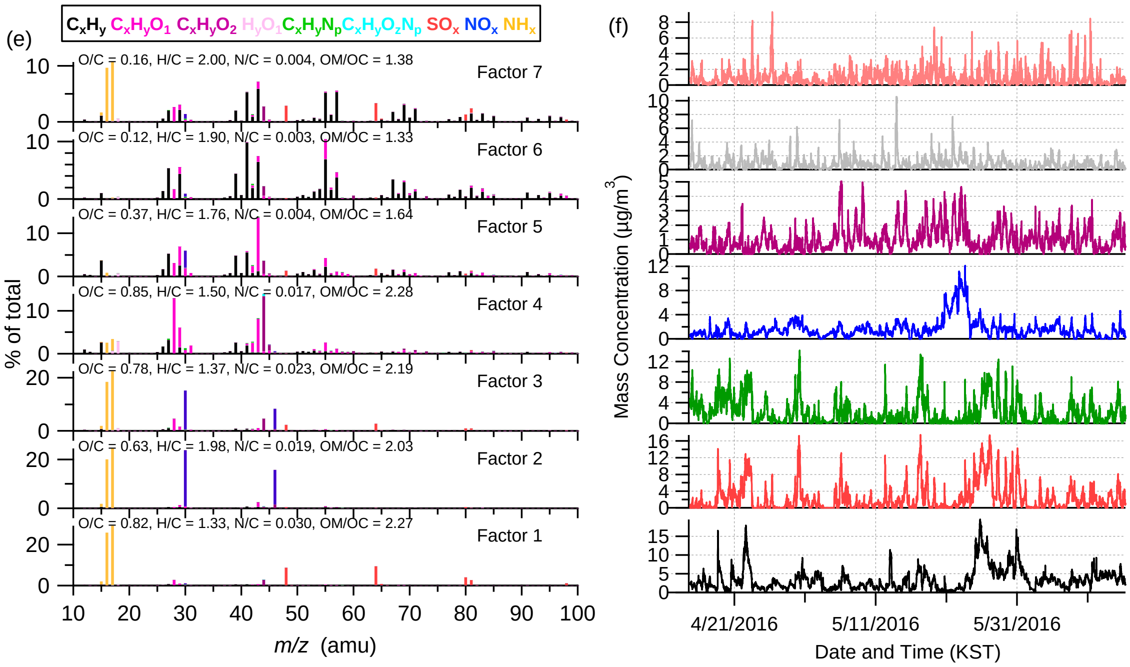

Figure S7. Overview of two other solution sets and 6-factor solution including inorganic factors and signals from inorganic included PMF analysis: **(a)(b)** High resolution mass spectra and time series of the different OA factors from the 5-factor solution (3-OA); **(c)(d)** High resolution mass spectra and time series of the different OA factors from the 6-factor solution (4-OA); **(e)(f)** High resolution mass spectra and time series of the different OA factors from the 7-factor solution (5-OA). The mass spectra are colored by different ion families.

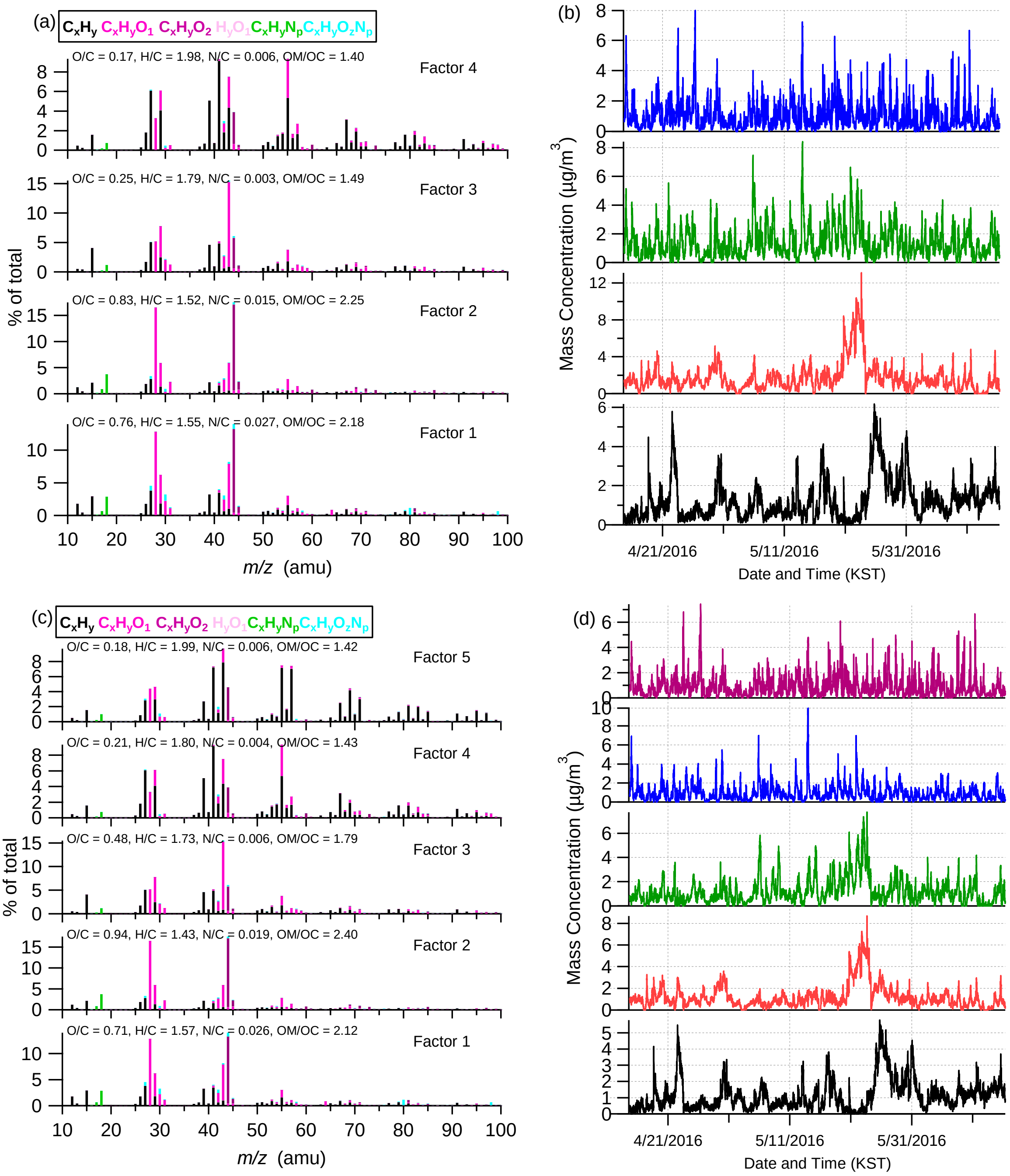

Figure S8. Overview of the 4-factor solution (**a** and **b**) and the 5-factor solution (**c** and **d**) from PMF analysis of the organic mass spectra only. The mass spectra are colored by different ion families.

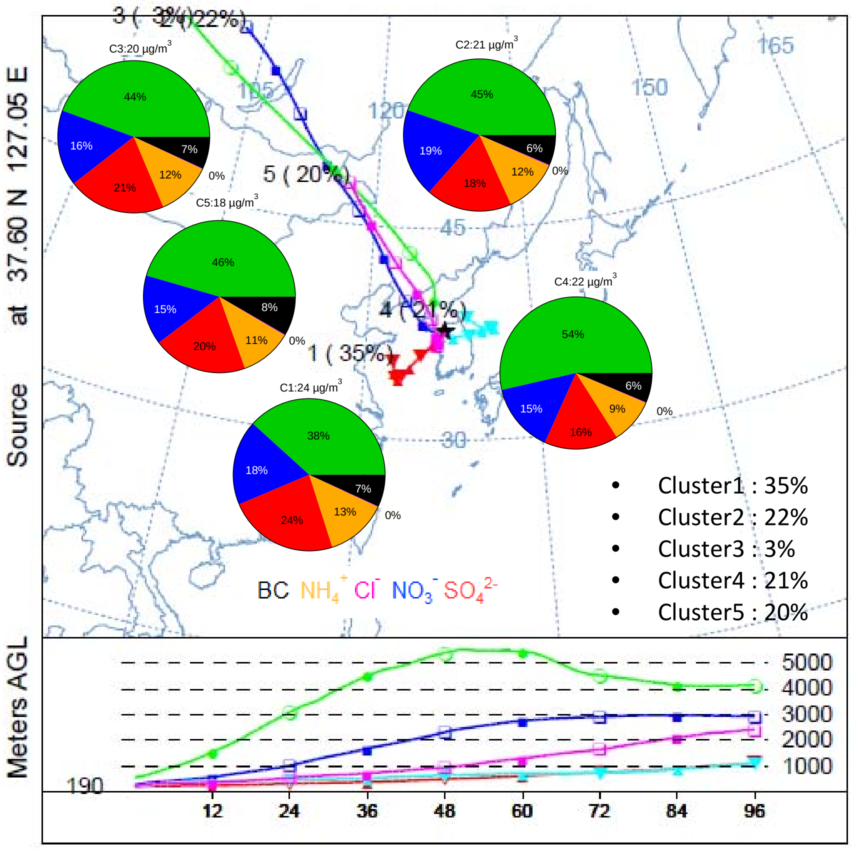

Figure S9. Averaged compositional pie chart of PM_1 species (non-refractory-PM_1 plus black carbon (BC)) in different clusters from the five cluster solution. The trajectories were released at half of the mixing height at the KIST (latitude: 37.60N; longitude: 127.05E) and the average arriving height for the back trajectories for this study was approximately 190 m.

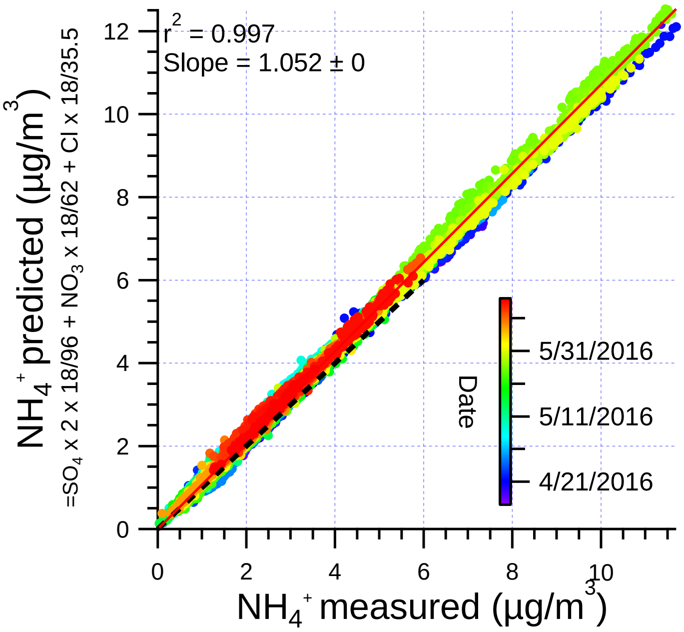

Figure S10. Scatterplot that compares predicted NH_4^+ versus measured NH_4^+ concentrations. The predicted values were calculated assuming full neutralization of the anions (e.g., sulfate, nitrate, and chloride). The data points are colored by date.

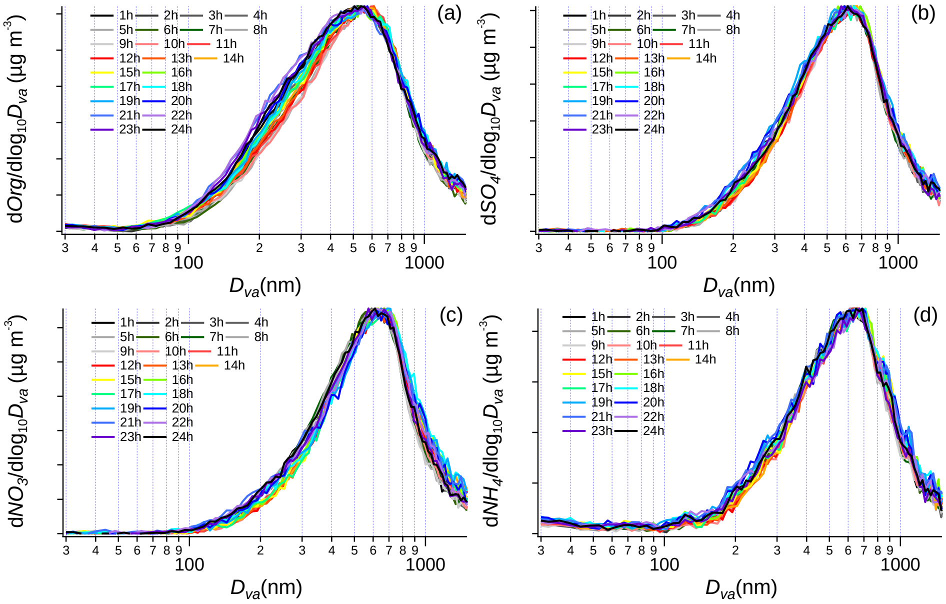

Figure S11. Size distributions for (a) organic; (b) Sulfate: (c) Nitrate; (d) ammonium for every hour. Y axis are shared for all distributions which are maximized to the axis.

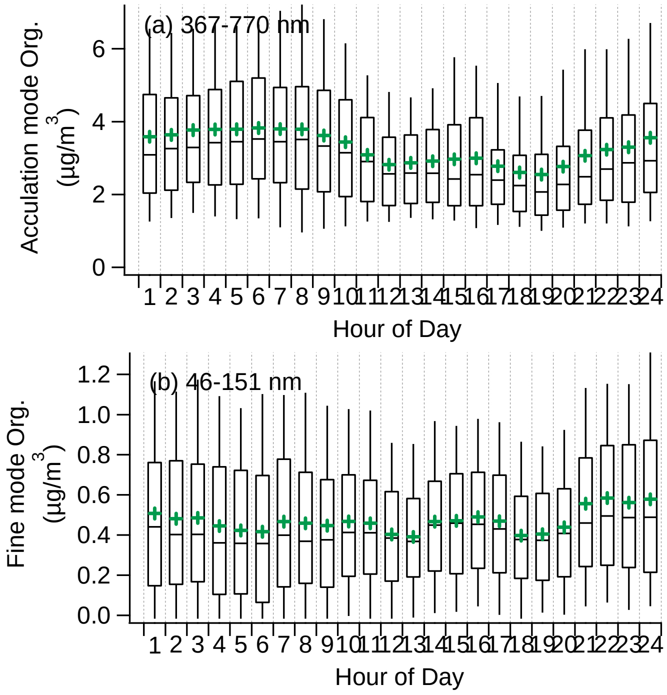

Figure S12. One-hour averaged diurnal profiles of organics in (a) accumulation mode and (b) fine mode.

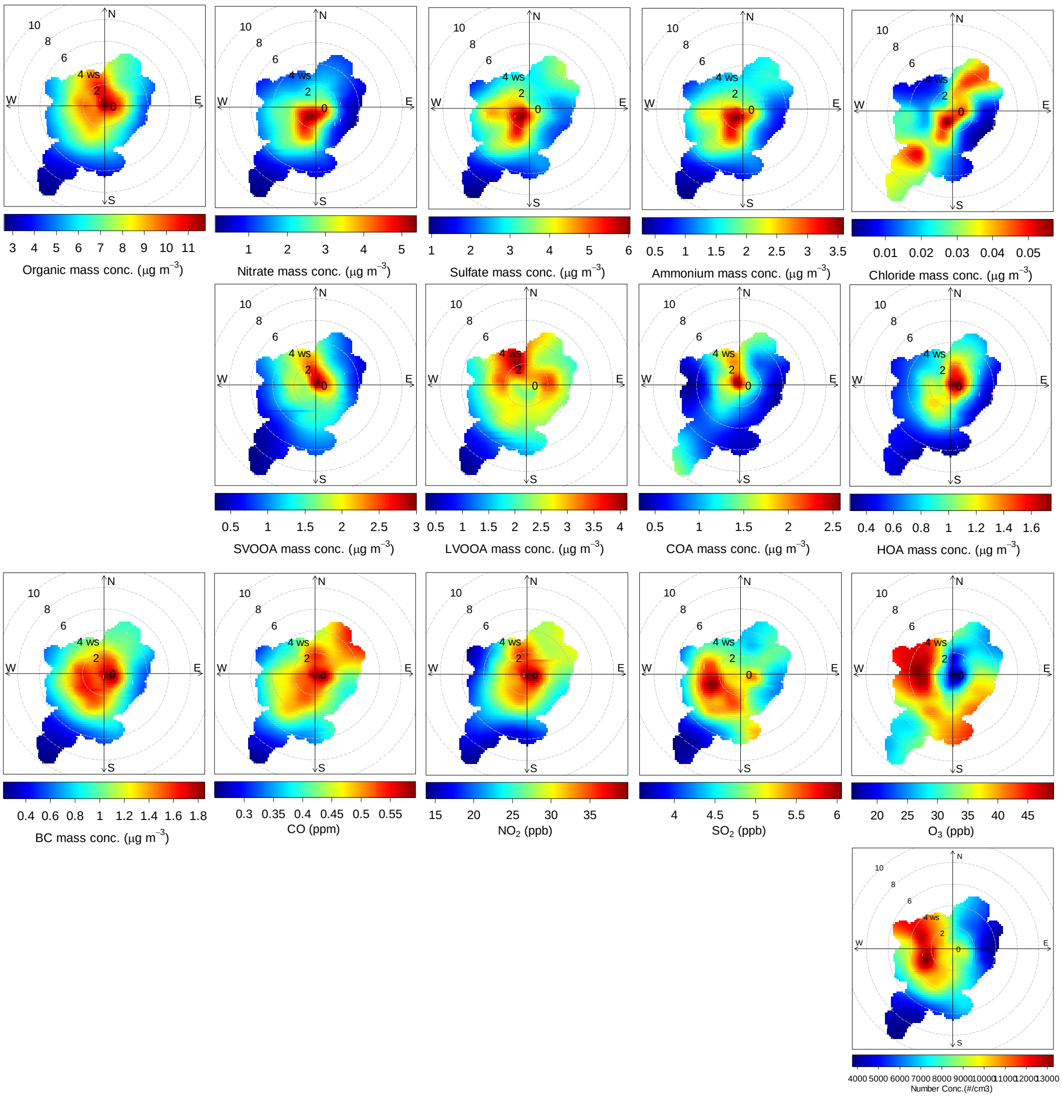

Figure S13. Polar plots of hourly averaged PM$_1$ species concentrations (top row), mass concentrations of the five OA factors identified from PMF analysis (middle row), the mixing ratios of various gas phase species (second row from the bottom), and the particle number concentrations (bottom row) as a function of WS and direction.

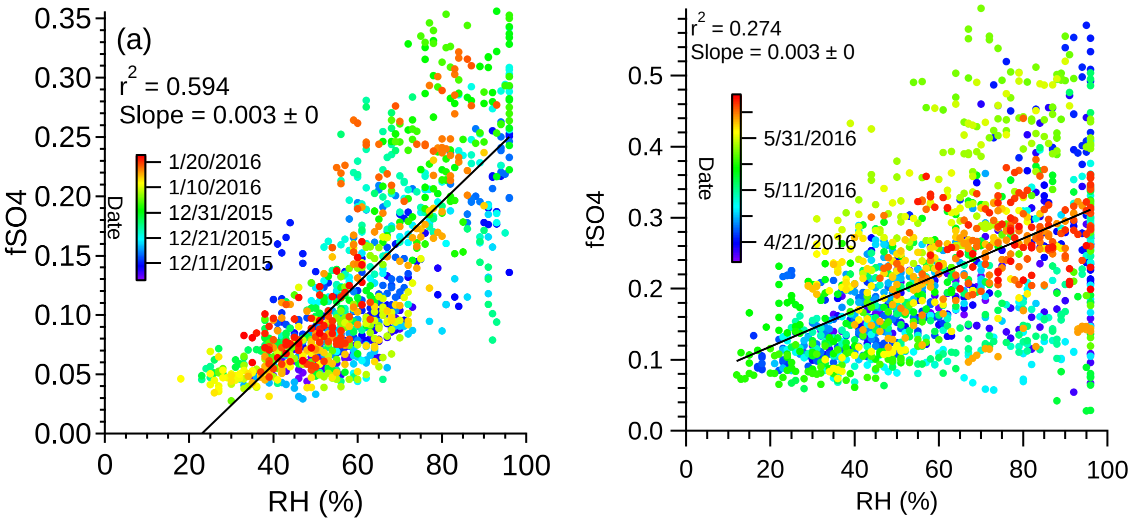

Figure S14. Scatterplot of the variations of fSO4 ratios as a function of RH **(a)** during winter (Kim et al., 2017); **(b)** during spring in this study.

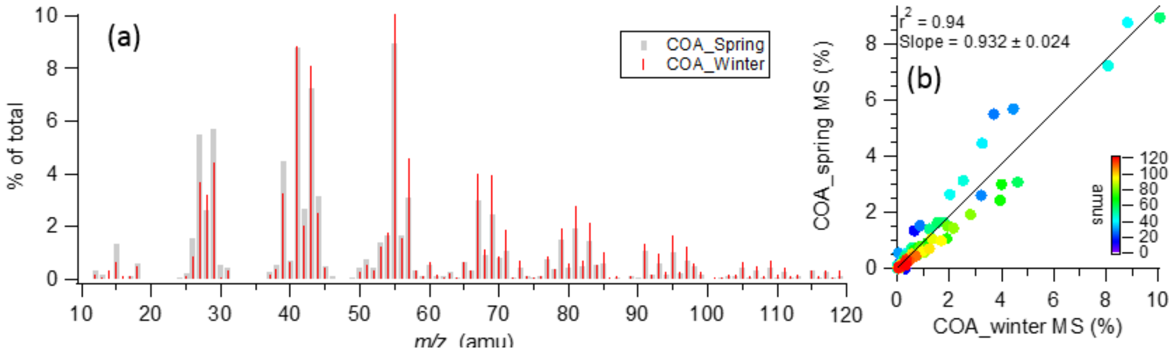

Figure S15. (a) Comparisons of mass spectra of the COAs from this study (spring) and the one from winter, 2015-2016; **(b)** scatter plots of both COA mass spectra

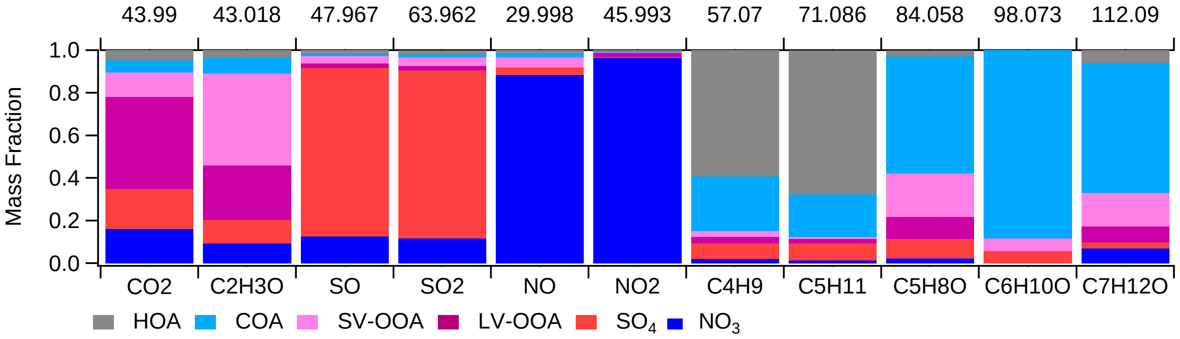

Figure S16. Mass fractional contribution of the factors (four OA factors + two inorganic factors) from PMF analysis to various ions that are relevant to each significant tracer.

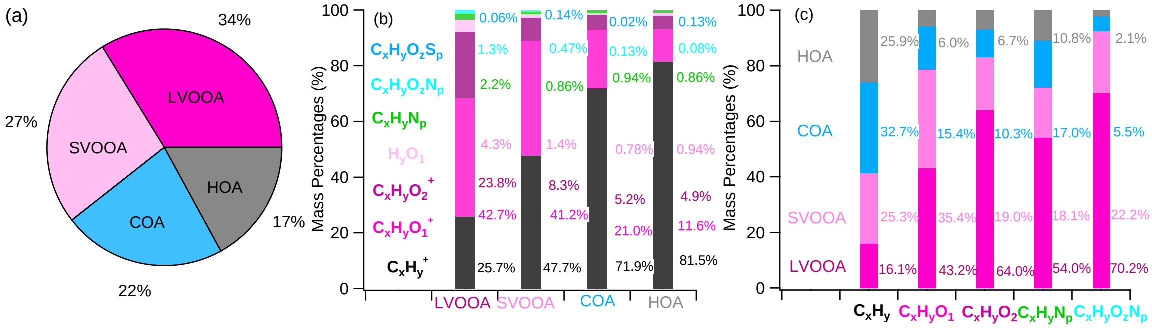

Figure S17. (a) Compositional pie chart of the average fractional contribution of each of the OA factors to the total OA over the campaign; **(b)** Average mass fractional contributions of seven ion families to each of the OA factors and; **(c)** Average mass fractional contributions of four OA factors to 4 each ion families

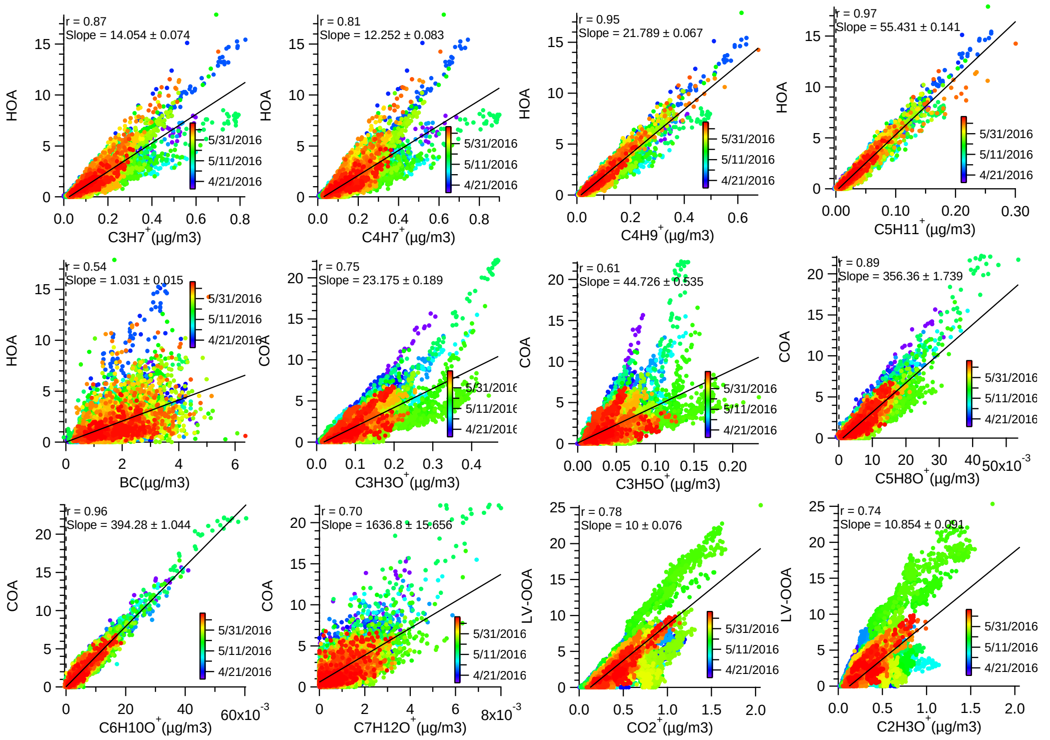

Figure S18. Scatter plots of OA factors and relevant tracer ions colored by measurement date.

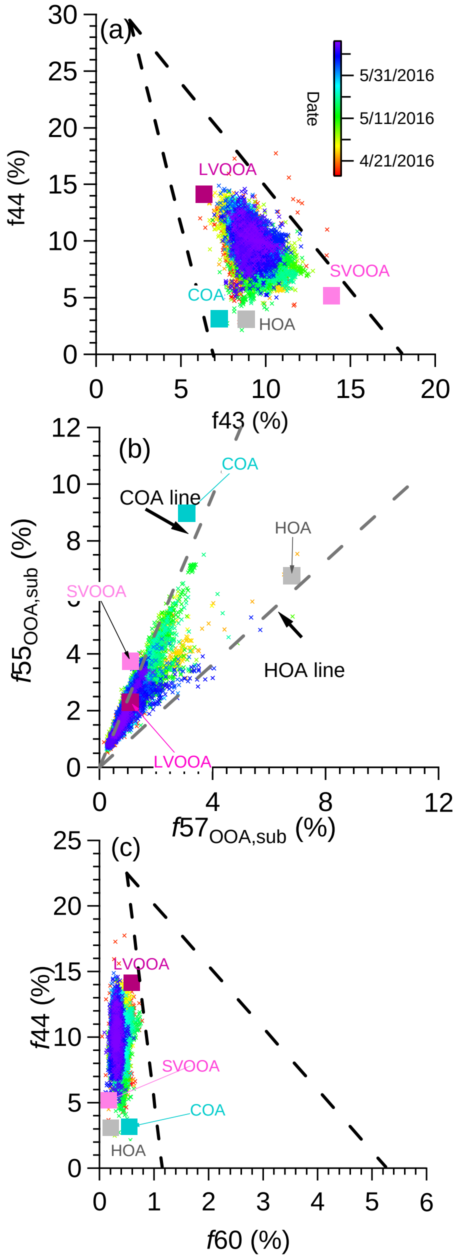

Figure S19. Triangular plots of **(a)** f_{44} versus f_{43} and **(b)** f_{44} versus f_{60} (c) $f_{55,\mathrm{OOA\ sub}}$ versus $f_{57,\mathrm{OOA\ sub}}$ for the five OA factors and all of the measured OA data (dots), colored by the time of the day. f_{43}, f_{44}, and f_{60} are the ratios of the organic signal at m/z = 43, 44, and 60 to the total organic signal in the component mass spectrum, respectively. $f_{55,\mathrm{OOA\ sub}}$ and $f_{55,\mathrm{OOA\ sub}}$ are the ratios of the organic signal at m/z 55, 57 after subtracting the contributions from SV-OOA and LV-OOA (e.g., $f_{55,\mathrm{OOA\ sub}} = m/z\ 55 - m/z55_{SV\text{-}OOA} - m/z55_{LV\text{-}OOA}$; $f_{57,\mathrm{OOA\ sub}} = m/z\ 57 - m/z\ 57_{SV\text{-}OOA} - m/z\ 57_{LV\text{-}OOA}$)

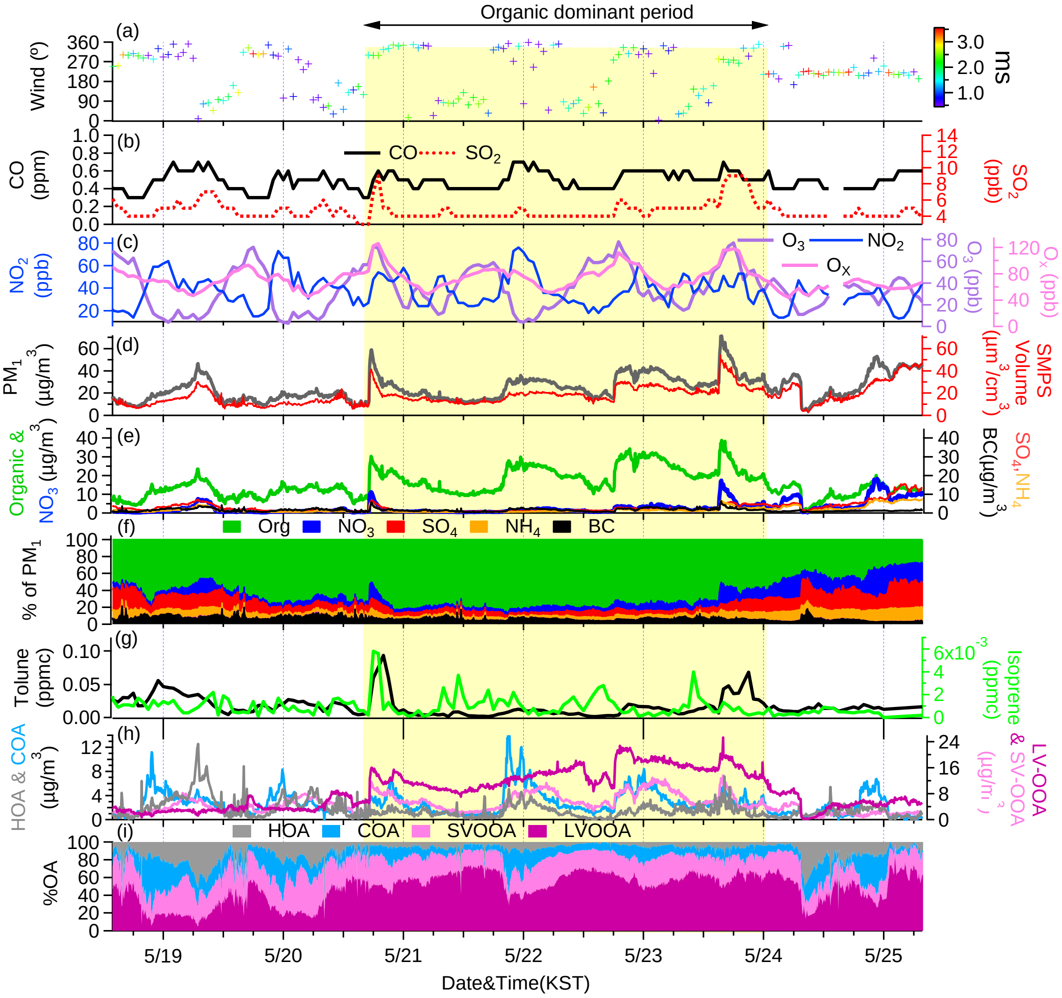

Figure S20. Overview of the temporal variations of submicron aerosols at the Korea Institute of Science and Technology (KIST) in SMA from May 19 to May 25 including organic dominant period colored by yellow (May 20, 17:00-May 24:0:00): **(a)** Time series of wind direction (WD), with colors showing different wind speeds (WS); **(b)** Time series of CO and SO_2; **(c)** Time series of O_3, NO_2 and O_x (NO_2+O_3); **(d)** Time series of total particulate matter (PM_1) and scanning mobility particle sizer (SMPS) volume concentrations; **(e)** Time series of the organic (Org.), nitrate (NO_3^-), sulfate (SO_4^{2-}) , ammonium (NH_4^+) and BC aerosols; **(f)** Time series of the mass fractional contribution of organic aerosols (Org.), nitrate (NO_3^-), sulfate (SO_4^{2-}), ammonium (NH_4^+) and BC to total PM_1; **(g)** Isoprene and toluene time series; **(h)** Time series of each factor derived from the positive matrix factorization (PMF) analysis; **(i)** Time series of the mass fractional contribution to total organic aerosol (OA).

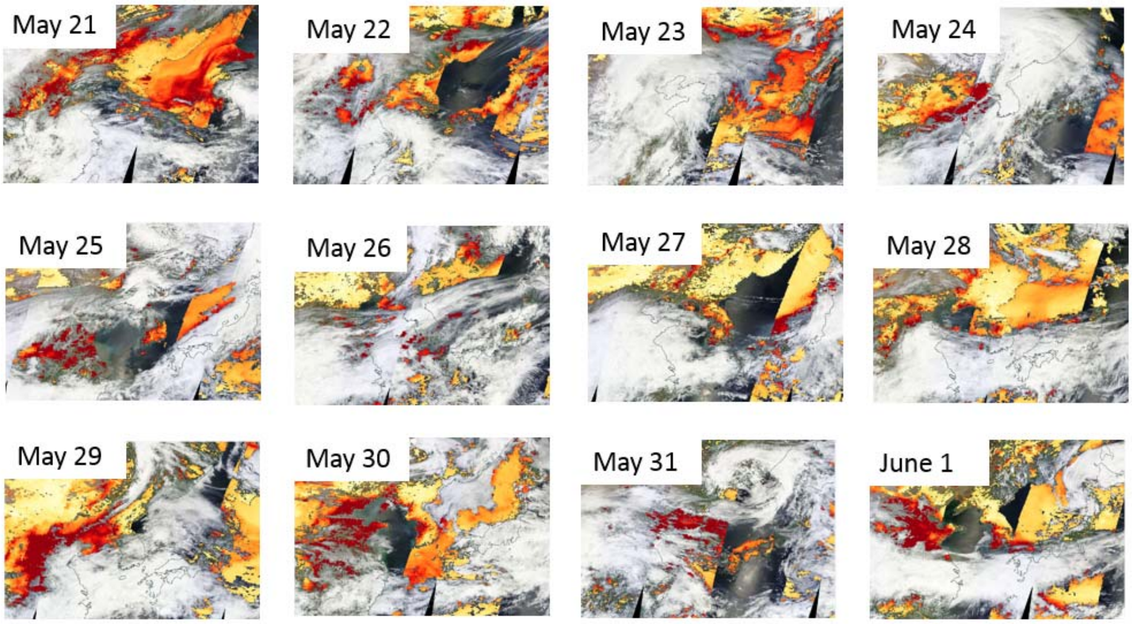

Figure S21. Long range transportation of plums from China to Korea during Haze period. Plots are from MODIS, terra.

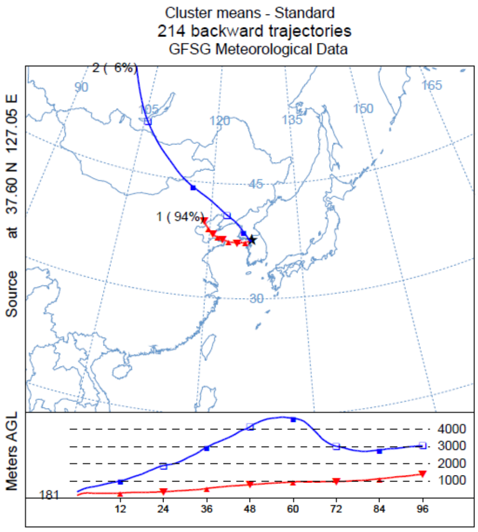

Figure S22. Two cluster solution of backtrajectroy analysis during haze period from (5/24 7:00-6/2 24:00). The trajectories were released at half of the mixing height at the KIST (latitude: 37.60N; longitude: 127.05E) and the average arriving height for the back trajectories for this study was approximately 181 m.

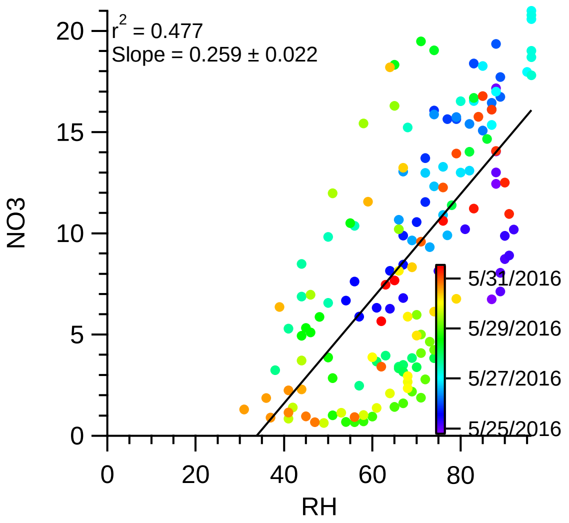

Figure S23. Scatterplots between nitrate vs. RH during haze period.

1. Properties of Organic sources

1.1 Hydrocarbon-like OA (HOA)

Alkyl fragments ($C_nH_{2n+1}^+$ and $C_nH_{2n-1}^+$) made a substantial contribution to the HOA spectrum, with major peaks at *m/z*'s 41, 43, 55, and 57 which were mostly composed of $C_3H_5^+$, $C_3H_7^+$, $C_4H_7^+$, and $C_4H_9^+$ ions, respectively (Fig. 8a). These major peaks and the overall picket fence fragmentation pattern resulting from the $C_nH_{2n+1}^+$ ions are typical features of the HOA spectra reported in other studies and are due to the association of these aerosols with fossil fuel combustion (e.g.,Alfarra et al., 2007;Lanz et al., 2008;Sun et al., 2011b;Zhang et al., 2005a;Huang et al., 2010;Morgan et al., 2010;Ng et al., 2011;Collier, 2015;Ge et al., 2012a;Kim et al., 2017;Young et al., 2016). In addition, strong correlations were observed between the time series of HOA and the $C_nH_{2n+1}^+$ and $C_nH_{2n-1}^+$ ions, e.g., $C_3H_7^+$ (r = 0.87), $C_4H_7^+$ (r = 0.81), $C_4H_9^+$ (r = 0.95), and $C_5H_{11}^+$ (r = 0.96) (Fig. S17 and Table 2). Due to the dominance of chemically reduced hydrocarbon species, the O/C ratio of the HOA was low (0.15), whereas the H/C ratio was high (2.00). On average, HOA contributed 17% of the total OA, which was similar to the number observed in winter (16 %) (Kim et al., 2017).

1.2 Cooking OA (COA)

COA has been widely reported in urban areas with high population densities (e.g., He et al., 2010;Huang et al., 2010;Mohr et al., 2012;Sun et al., 2011b;Young et al., 2016;Ge et al., 2012a;Wang et al., 2016b;Xu et al., 2014;Hayes et al., 2013). In this study, COA was found to account for 22% of the total OA mass, higher than HOA (Fig. S16). The diurnal pattern of COA displayed a large enhancement at evening starting from ~ 19:00, i.e., dinner time, and a small lunch time peak at ~ 12:00. Elevated COA concentration and larger fractional contribution to OA mass were observed throughout the night (Figs. 3 and 8f).

Similar to HOA, the mass spectrum of COA contained many alkyl fragments, but to a lesser extent (71.9 % of the total signal in COA spectrum compared to 81.5 % of the total signal in HOA spectrum) (Fig. S16). COA also contained significantly larger amounts of oxygen containing ions than HOA (e.g., $C_xH_yO_1^+$ = 21.0% vs. 11.5% and $C_xH_yO_2^+$ = 5.2% vs. 4.9%) (Fig. S16), and thus had a higher O/C ratio (0.19 vs 0.15) and a lower H/C ratio (1.83 vs. 2.00). The O/C ratio (0.19) of COA in spring was found to be higher than that in winter (0.14) but both values were within the range of the O/C ratios of COA observed in other studies (e.g., Barcelona (0.27) (Mohr et al., 2012), New York City (NYC) (0.23) (Sun et al., 2011a) and Fresno (0.14 in 2010 (Ge et al., 2012b) and 0.19 in 2013 (Young et al., 2016)). Key tracers for identifying the presence of aerosols from cooking related activities, such as $C_3H_3O^+$ (*m/z* 55), $C_3H_5O^+$ (*m/z* 57), $C_5H_8O^+$ (*m/z* 84) and $C_6H_{10}O^+$ (*m/z* 98) (He et al., 2004;Adhikary et al., 2010;Mohr et al., 2009;Zhao et al., 2007;Ge et al., 2012a;Sun et al., 2011b), all showed good correlation in time series with COA, e.g., $C_3H_3O^+$ (r = 0.75), $C_3H_5O^+$ (r = 0.61), $C_5H_8O^+$ (r = 0.89), $C_7H_{12}O^+$ (r = 0.70), and $C_6H_{10}O^+$ (r = 0.99) (Fig. S17 and Table 2) and COA was a major contributor to the signals of $C_5H_8O^+$, $C_6H_{10}O^+$, and $C_7H_{12}O^+$, accounting for 62%, 94%, and 67%, respectively, of their signals (Fig. S15). Finally, the ratios between *f*55 and *f*57 for OA in Seoul increased proportionally as the fractional contribution of COA to total OA increased (Fig. S18b), with a "V" shape indicated by the two edges defined by the COA and the HOA factors from several urban AMS data sets (Mohr et al., 2012). These observations all confirm the identification of COA at SMA.

1.3. Semi-volatile and low volatile oxygenated OA (SV-OOA and LV-OOA)

In addition to the two POA factors, two OOA factors were identified and were found to account for an average of 61% of the OA mass (Fig. S16a) with LV-OOA and SV-OOA being 34 and 27%, respectively. OOA is ubiquitous in the atmosphere and usually a dominant component of submicrometer particles (Jimenez et al., 2009;Zhang et al., 2007). SOA formation was more important in spring that in winter: OOA contributed an average 61% of the OA mass in this study but only 41% during winter. In addition, the average OOA concentration in this study was higher than in winter (5.9 vs. 4.9 μg m^{-3}).

CO_2^+ (*m/z* 44) and $C_2H_3O^+$ (*m/z* 43) were major fragments of oxidized organics and therefore frequently used as key tracers for identifying the presence of SOA in absence of biomass burning influence. In this study, the time series of SV-OOA and LV-OOA correlated well with these ions, e.g., LV-OOA vs CO_2^+ (r = 0.78), SV-OOA vs $C_2H_3O^+$ (r = 0.89) (Figs. S17 and Table 2). As shown in the triangle plots in Fig. S18, SV-OOA (O/C = 0.56; H/C = 1.90) resides within the region representing fresher SOA, with a low f_{44}. The mass spectrum of SV-OOA is characterized by two prominent peaks, *m/z* 29 (mainly CHO^+) and *m/z* 43 (mainly $C_2H_3O^+$) (Fig. 8c). In addition, the SV-OOA show high fraction of $C_xH_yO_1^+$ family (41 %), most likely from carbonyl or alcohol functional groups, while much lower contribution of $C_xH_yO_2^+$ family (8.3 %), mainly from carboxylic functional groups (Fig. S16b). The diurnal variation of SV-OOA shows higher concentrations at night and lower concentrations at daytime with a small afternoon peak

(Fig. 8g). The mass spectral features and diurnal variation of SV-OOA suggest that this factor was driven by the partitioning of semivolatile organics between gas and particle phase and that SV-OOA formation was facilitated by the high humidity and low temperature during nighttime. In addition, SV-OOA appeared to represent relatively fresh SOA formed from photochemical reactions during daytime (Docherty et al., 2011). Indeed, a decrease of the PBL height, thus less dilution, together with continued reactions of VOCs with the nighttime residual ozone (20–35 ppb on average; Fig. 3) and other oxidants (e.g., nitrate radical) might have played a role in the production of semivolatile secondary organic species at night. This kind of formation processes also suggests that SV-OOA was mostly formed locally. Indeed, the polar plot of SV-OOA showed that its high concentrations tended to be associated with lower wind speed.

On the other hand, the LV-OOA factor is characterized by high O/C ratio (=0.91) (Fig. 8d) and high f_{44} (14 %) (Fig. S18a), which are in similar range as those previously reported for aged and highly oxidized OA, including LV-OOAs, from various locations (e.g., Hayes et al., 2013;Mohr et al., 2012;Zhang et al., 2014;Ng et al., 2010). The diurnal profile of LV-OOA was different than SV-OOA as well, showing a gradual increase from 8:00 till late afternoon despite a rising PBL height (Fig. 8h). This diurnal pattern was very similar to O_x ($O_x = O_3+NO_2$) (Fig. 8). In fact, LV-OOA correlated positively with O_x ($r = 0.57$; Fig. S19) and the correlation was higher ($r = 0.60$; Fig. 9) between 10:00 and 16:00 when photochemical processing was intense. Note that a high organic period (May 20-May 23) was excluded in this correlation because it appeared to be driven by processes that were different than the other periods thus showed substantially higher LV-OOA/O_3 ratios than the rest of the study (Fig. 9). Details on this episode is discussed in section 3.4. Unless otherwise indicated, the high organic period (May 20-May 23) was excluded from the O_x vs. OOA, LV-OOA and SV-OOA correlations. The relatively good correlation between LV-OOA and O_x during daytime indicates that LV-OOA corresponded to photochemically produced SOA (Fig. 8d). Furthermore, a gradual increase starting from ~08:00 till late afternoon indicated that the photochemical production was coupled with transport of air masses from regions outside of SMA. Indeed, the diurnal profile of ozone at the KIST site demonstrated a peak between 16:00–17:00 (Figs. 3,8) associated with southwesterly winds that transported ozone produced outside of SMA coupled with local daytime photochemical production. The high O/C (0.91) of the LV-OOA as well as a dispersed feature of its polar plot (Fig. S12) all support the regional secondary characteristics of LV-OOA.

References

Aiken, A. C., Decarlo, P. F., Kroll, J. H., Worsnop, D. R., Huffman, J. A., Docherty, K. S., Ulbrich, I. M., Mohr, C., Kimmel, J. R., Sueper, D., Sun, Y., Zhang, Q., Trimborn, A., Northway, M., Ziemann, P. J., Canagaratna, M. R., Onasch, T. B., Alfarra, M. R., Prevot, A. S. H., Dommen, J., Duplissy, J., Metzger, A., Baltensperger, U., and Jimenez, J. L.: O/C and OM/OC ratios of primary, secondary, and ambient organic aerosols with high-resolution time-of-flight aerosol mass spectrometry, Environmental Science & Technology, 42, 4478-4485, 10.1021/es703009q, 2008.

Canagaratna, M. R., Jimenez, J. L., Kroll, J. H., Chen, Q., Kessler, S. H., Massoli, P., Hildebrandt Ruiz, L., Fortner, E., Williams, L. R., Wilson, K. R., Surratt, J. D., Donahue, N. M., Jayne, J. T., and Worsnop, D. R.: Elemental ratio measurements of organic compounds using aerosol mass spectrometry: characterization, improved calibration, and implications, Atmospheric Chemistry and Physics, 15, 253-272, 10.5194/acp-15-253-2015, 2015.

Kim, H., Zhang, Q., Bae, G. N., Kim, J. Y., and Lee, S. B.: Sources and atmospheric processing of winter aerosols in Seoul, Korea: insights from real-time measurements using a high-resolution aerosol mass spectrometer, Atmos. Chem. Phys., 17, 2009-2033, 10.5194/acp-17-2009-2017, 2017.

Kuwata, M., Zorn, S. R., and Martin, S. T.: Using Elemental Ratios to Predict the Density of Organic Material Composed of Carbon, Hydrogen, and Oxygen, Environmental Science & Technology, 46, 787-794, 10.1021/es202525q, 2012.

Middlebrook, A. M., Bahreini, R., Jimenez, J. L., and Canagaratna, M. R.: Evaluation of Composition-Dependent Collection Efficiencies for the Aerodyne Aerosol Mass Spectrometer using Field Data, Aerosol Science and Technology, 46, 258-271, 10.1080/02786826.2011.620041, 2012.

Zhang, Q., Canagaratna, M. R., Jayne, J. T., Worsnop, D. R., and Jimenez, J. L.: Time- and size-resolved chemical composition of submicron particles in Pittsburgh: Implications for aerosol sources and processes, Journal of Geophysical Research-Atmospheres, 110, 10.1029/2004jd004649, 2005.